Aeroelastic implications of active winglet concept aimed to improve civil transport aircraft performances

Martin Delavenne, Bernard Barriety, Fabio Vetrano, Valérie Ferrand, Michel Salaün

AeroBest 2021
Lisboa, 21-23 July 2021

AEROELASTIC IMPLICATIONS OF ACTIVE WINGLET CONCEPT AIMED TO IMPROVE CIVIL TRANSPORT AIRCRAFT PERFORMANCES

Martin Delavenne[1*], Bernard Barriety[2], Fabio Vetrano[2], Valérie Ferrand[3] and Michel Salaün[4]

1: Aircraft Design Department
ISAE-Supaero
Univ. Toulouse
10 Av. Edouard Belin, Toulouse, France
martin.delavenne@isae-supaero.fr

2: Loads and Aeroelastic Department
Airbus Operations SAS
316 route de Bayonne, Toulouse, France

3: Aerodynamic and Propulsion Department
ISAE-Supaero

4: Structural Mechanics and Material Department
ISAE-Supaero

Abstract. *Reduction of aircraft environmental footprint has become over years a key objective for the industry. Particularly, for decades winglets have been proven to efficiently reduce drag and fuel consumption. However, the design of those wingtip extensions mainly relies on an aerodynamic shape optimisation for a given cruise condition resulting in suboptimal behaviour for the rest of the flight. Active winglet concept proposes to optimise the winglet cant angle along the flight to compensate the loss of efficiency inherent to fixed designs. The variation of winglet deflection impacts the lift distribution with repercussion on wing deformation that must be investigated. Besides, the presence of moving masses at the tip of the wing also has influence on dynamic response and particularly on flutter onset. This work proposes to evaluate those impacts through an aeroelastic analysis of both static and dynamic implications of active winglets combined with an aerodynamic performances optimisation. The XRF1, an Airbus provided industrial standard multi-disciplinary research test case representing a typical configuration for wide body long-range aircraft, is used as the baseline aircraft. Coupled CFD/CSM computations are performed to assess the evolution of wing shape with respect to winglets deflections and the consequences on mission performance optimisation. While a parametric flutter analysis is carried-out to highlight the dependence of critical flutter speed on winglet cant angle.*

Keywords: Active winglet, aeroelasticity, CFD/CSM, optimization

1 INTRODUCTION

In a context that urges aeronautical industry to reduce its environmental footprint, new solutions must be considered to improve aircraft performances. Historically, as illustrated in Fig.1 the increase of wings aspect ratio has been one of the preferred solution to improve the aerodynamic efficiency. Indeed, according to Prandtl's work [1] induced drag – that is responsible for more than one third of the total drag – is inversely proportional to the aspect ratio. However, this growth was limited by airports regulations on maximum span and the detrimental impact of high aspect ratio wings on structural weight. To overcome these limits winglets have been introduced in the 1970s and led to drag reduction by around 4% with limited impact on weight [2, 3]. More recently, the massive deployment of composite materials combined with folding wing-tips and loads alleviation devices (active or passive) allow for high aspect ratio wings without compromising ground operations nor structural weight [4–6].

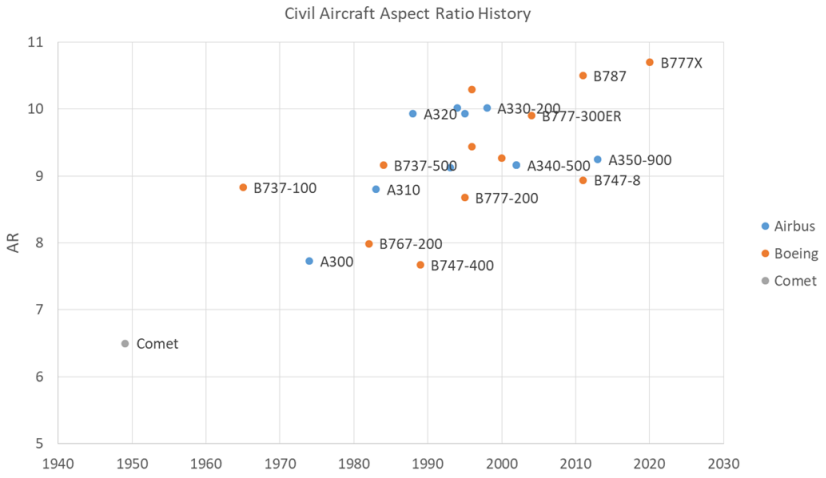

Figure 1: Aircraft aspect ratio constantly increases with years

However, the aerodynamic design approach that relies on fixed shapes optimised for a given flight condition must be challenged. Indeed, it can be shown that single point optimisation leads to suboptimal performances in the remaining of the flight domain with detrimental impact on fuel burnt [7]. The same source indicates that multipoint optimisation that considers static aeroelastic deformation is part of the solution to improve performances within the operational envelop but, as the wing shapes is still frozen at design stage, a slight overconsumption will persist. Morphing wing technologies [8] that relies on continuous shape adaptation appear as providential solutions. As Prandtl demonstrated in the 1920s [1], induced drag is directly related to the spanwise lift distribution. Its optimisation with active devices such as NASA's VCCTEF (Variable Camber Continuous Trailing Edge Flap) could lead to improvements of the aerodynamic efficiency by more than 5% [9, 10]. Additional gains are also to be expected from the loads alleviation and flutter control provided by these technologies. However, they may suffer from certification and maintenance issues as well as weight penalties from actuation system [11].

Active winglet patented by Airbus [12] consists in a winglet whose cant angle (δ) can change during the flight as illustrated in Fig.2. It takes advantage of higher aspect ratio wings and morphing technologies while limiting their downsides: It allows for higher span

Figure 2: Active winglet principle with variable cant angle.

without impact on ground operations and provides a mean to actively control the lift distribution with a simple actuation system. Loads alleviation capabilities have also been demonstrated and ensure a limited impact on structural weight [13]. First assessments of the benefits of the device have been carried out on the XRF1 – an Airbus provided industrial standard multidisciplinary research test case representing a typical configuration for wide body long range aircraft – equipped with retrofitted winglets [14, 15]. They highlighted the necessity to consider not only aerodynamic performances but also structural deformations through coupled approaches like CFD/CSM (Computational Fluid Dynamics / Computational Structural Mechanics) computations. It has indeed been shown that wing flexibility could drastically alter the efficiency of the device [14]. Consequently, fuel saving expectations are brought from 2% when only aerodynamics is considered [16] to less than 1% when coupled computations are carried out. In the present paper, surrogate-based mission analysis is extended to a XRF1 high aspect ratio wing configuration [17] and compared to the XRF1 with retrofitted optimised active winglets configuration [15]. The impact of the static aeroelastic deformations on the efficiency of the device perceived in [14] is detailed. Finally, the implications on flutter onset of moving masses at the tip of the wing are explored.

2 NUMERICAL METHODS

As mentioned in the introduction, the entire approach relies on coupled CFD/CSM computations aimed to assess the aerodynamic performances while considering wing deformations. This section provides details about both aerodynamic and structural models involved in the analysis. The surrogate model based mission analysis procedure is also presented.

2.1 XRF1 Test cases

Figure 3 presents the two test cases considered for this study: The XRF1 configuration with a retrofitted optimised winglet [15] and the high aspect ratio configuration equipped with a folding wing-tip. Hinges are respectively located at winglet root and at maximum span limit for this aircraft category i.e. 32m. The wing-tip size of the high aspect ratio configuration can be extended by moving the hinge inward down to 30m. Because of the wing size extension the maximum take-off weight (MTOW) and the operational weight empty (OWE) are increased by respectively 0.5% and 4.6% for the high aspect ratio configuration with respect to baseline XRF1. The wing reference surface also raises by almost 8%.

(a) XRF1 plus winglet configuration (b) XRF1 high aspect ratio configuration

Figure 3: XRF1 configurations used in this study.

2.2 Aerodynamic computations

The aerodynamic performances are assessed using the DLR CFD code TAU [18]. RANS equations are solved for an unstructured mesh (Figure 4) of about 5 millions nodes with Menter-SST turbulence model. It can be shown [15] that the analysis of a simplified model only composed of the wing is sufficient to capture the effects of winglet cant variation on drag. This simplification is applied for the remainder of this study. For flutter assessment

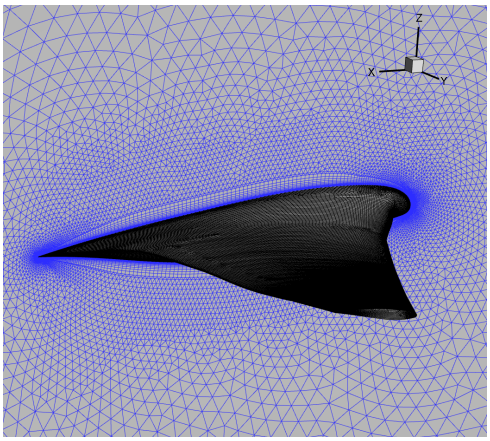

Figure 4: Example of unstructure mesh for the XRF1 wing

unsteady aerodynamics forces in the frequency domain must be considered. They are computed using Linearised Frequency Domain (LFD) method. The method relies on a linearisation of the RANS equations around a non-linear steady state considering small harmonic disturbances [19]. It allows to capture non-linearities such as shocks and flow separations and has been developed to capture flutter boundaries more accurately while maintaining a reasonable computational cost.

2.3 Structural computations

The structural displacements are computed with Finite Element Method. A wing model composed of approximately 300,000 degrees of freedom is considered as illustrated on Fig.5 for both XRF1 wing configurations. The wing is considered to be clamped at the root rib. The material is aluminium and the weight of non-structural elements such as fuel are taken into account through punctual masses distributed along the span. The weight of the actuation system is estimated to 140kg based on scaling of the Valkyrie folding wing-tip mechanism [20]. The stiffness of the actuation system is not considered and rigid links are assumed between the fixed part of the wing and the movable one. Both linear static and modal analyses are performed with MSC Nastran software [21] using respectively solutions SOL101 and SOL103 with a truncation to consider only the first 25 modes.

(a) XRF1 wing FEM (b) XRF1 high aspect ratio FEM

Figure 5: Finite elements models for XRF1 test cases wings.

2.4 Flutter computations

In this study, the consequences of winglet cant angle (δ) deflections on flutter boundaries must be investigated. Indeed, changing significantly tip masses location is likely to have influence on flutter critical speed. To know whether this change increases or reduces margins is of first importance regarding aircraft safety. Flutter equation (1) must be solved for frequencies within the range of interest and every cant angle deflections.

$$-\mathbf{M}\omega^2 + i\mathbf{D}\omega + \mathbf{K} = \mathbf{Q} \tag{1}$$

The generalised aerodynamic forces $\mathbf{Q}$ are extracted from LFD computations. Because they depend on the frequency itself the eigenvalue problem must be solved iteratively. In this study, the p-k method is used [22]. The reduced frequencies k, that is computed from reference chord c and aircraft speed V such as $k = \frac{\omega c}{V}$, ranges from 0 to 4.0.

2.5 Surrogate based mission analysis

The evaluation of the mission performances relies on surrogate models built from CFD/CSM computations. A full-factorial design of experiment (DoE) composed of $n = 126$ samples ($\vec{x_i}$) is generated with aircraft mass, cruise altitude and cant deflection as parameters ($N = 3$). The range of each of them is indicated in Tab.1 with MZFW being the maximum zero fuel weight of the aircraft and MTOW its maximum take-off weight.

Table 1: Full-factorial design of experiment parameters ranges.

Param.	Lower Bound	Upper Bound
δ (deg)	-90	90
Altitude (ft)	30000	41000
Weight	MZFW	MTOW

Several surrogate models ($\hat{f}(\vec{x})$) have been tested to capture drag coefficient (C_D) and wing twist deformation ($\Delta\theta_{wing}$) evolutions with DoE parameters:

- Response Surface Model - RSM (p-polynomial)[23]:
  $\hat{f}(\vec{x}) = \beta_0 + \sum_{i_1=1}^{n} \beta_{i_1} x_{i_1} + \sum_{i_1=1}^{n} \sum_{i_2 \leq i_1}^{n} \beta_{i_1 i_2} x_{i_1} x_{i_2} + ... + \sum_{i_1=1}^{n} ... \sum_{i_p \leq i_{p-1}}^{n} \beta_{i_1 ... i_p} x_{i_1} ... x_{i_p}$

- Gaussian Radial Basis Function - RBF [23]:
  $\hat{f}(\vec{x}) = \sum_{i=1}^{n} \beta_i \psi(\vec{x} - \vec{x_i})$ with $\psi(\vec{x}) = \exp(\frac{-||\vec{x}||^2}{2\sigma})$ – In this model σ is selected to minimize the cross-validation error.

- Ordinary Kriging [24]:
  $\hat{f}(\vec{x}) = \mu + \sum_{i=1}^{n} \beta_i \psi(\vec{x} - \vec{x_i})$ with $\psi(\vec{x} - \vec{x_i}) = exp[-\sum_{j=1}^{N} \theta_j |x_{,j} - x_{i,j}|^{p_j}]$ – In this model θ_j and p_j are parameters determine such that the model fit the sampling points.

The selection of the model is operated using cross-validation as detailed in [23]. The quality metrics Normalised Root Mean Square Error and the coefficient of determination R^2 are computed and compared for each model technique. Table 2 summarises the results of the cross-validation applied to the three pre-cited models and shows that kriging better performs and is the preferred choice.

Table 2: Validation and selection of drag and wing twist models

Model	NRMSE	R^2
C_D RSM	3.8×10^{-2}	0.972
C_D RBF	3.4×10^{-2}	0.982
C_D Kriging	$\mathbf{1.2 \times 10^{-4}}$	**0.999**
$\Delta\theta_{wing}$ RSM	4.87×10^{-2}	0.959
$\Delta\theta_{wing}$ RBF	2.02×10^{-2}	0.991
$\Delta\theta_{wing}$ Kriging	$\mathbf{6.6 \times 10^{-3}}$	**0.998**

Once the models have been built, the mission computation is performed. The cruise is cut in segments as illustrated in Fig.6. The drag on this segment (D_s) is computed and optimised from the model considering the weight and the altitude and changing winglet cant angle. The necessary thrust to maintain level flight is deduced and used to compute fuel consumption ($W_{fuel,s}$) and weight at the end of the segment. The process is iterated to ensure that starting weight fits with aircraft maximum take-off weight.

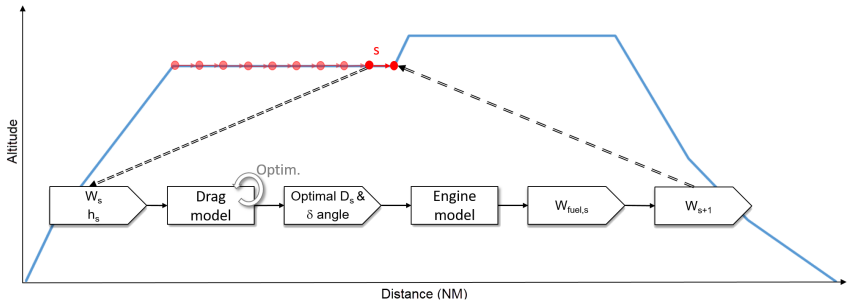

Figure 6: Mission cruise performance optimisation procedure.

3 STATIC AEROELASTIC DEFORMATIONS IMPACT ON PERFORMANCES

3.1 Active winglet efficiency

The active winglet efficiency is evaluated computing the reduction of fuel consumption for the two XRF1 test cases considering 500 different mission flight paths (range, altitudes) and payload combinations. The evolution of active winglet efficiency with mission range is presented in Fig.7a for both configurations. Figure 7b highlights its dependence on mean cruise altitude.

The first observation that can be drawn is the similarity between the two configurations. Despite the difference in term of wing design, the active winglet maximum efficiency seems to be roughly identical and does not exceed 1%. More difference appears when considering mean value, even small it reaches around 0.3% for high aspect ratio case while it is almost null for the configuration with retrofitted winglet. Indeed, negative

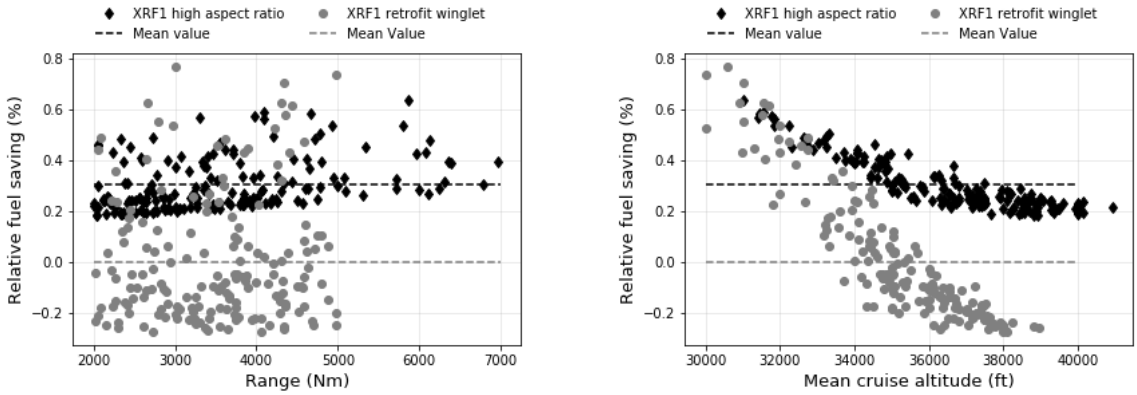

(a) Mission range

(b) Cruise mean altitude

Figure 7: Mission fuel consumption reduction with active winglets depending on flight range and mean altitude.

fuel savings i.e. overconsumption are observed for this latter case. They originate from the additional weight of the actuation system. In the retrofitted case the reference for comparison is the XRF1 equipped with a fixed optimised winglet without any actuator. For the high aspect ratio the reference is the same wing but equipped with a folding wing-tip only active on ground (deployed in flight) therefore with an actuation system already existing. Computation without consideration about the actuation weight have been carried out and show positive average fuel savings [15].

Figure 7a shows little dependency of fuel savings on mission range. But, considering the variation with respect to mean flight altitude in Fig.7b a trend emerges: The lower the flight the larger the benefits of active winglets. More details about the phenomenon at stake are provided in next paragraph.

3.2 Influence of static aeroelastic deformation

Maximum values of active winglet efficiency demonstrated so far are distant from what could have been expected from the literature [16]. This major difference lies on the flexibility of the wing that produces antagonist effects and reduce drag sensitivity to winglet cant angle variation. To explain implications of static aeroelastic deformations on active winglet efficiency the dependence of local angle of attack (AoA) on the winglet on cant variation and wing deformation must be considered. It could be decomposed into two parts:

- A rigid part dependent on global angle of attack α_∞, wing dihedral angle δ_{wing}, winglet cant angle δ and winglet twist $\theta_{winglet}$:

$$\alpha_{winglet_r} = \alpha_\infty \cos(\delta + \delta_{wing}) + \theta_{winglet} \tag{2}$$

- A flexible part dependent on wing tip static aeroelastic twist deformation $\Delta\theta_{wing}(\eta = 1)$, wing dihedral angle δ_{wing} and winglet cant angle δ:

$$\alpha_{winglet_f} = \sin^{-1}[\sin(\Delta\theta_{wing}(\eta = 1)) \cos(\delta + \delta_{wing})] \tag{3}$$

Rigorously, δ_{wing} contains a flexible part that results from the bending deformation. However, because the variation of dihedral angle due to wing deformation is small in front of cant angle variations its impact can be neglected.

Considering rigid wing, the lift distribution will only be affected by winglet folding. According to (2): $\lim_{|\delta|\to 90} \alpha_{winglet_r} \approx \theta_{winglet}$. Besides α_∞ tends to decrease with δ. Then, in cruise conditions because these two values are of the same order of magnitude the variation of local angle of attack on the winglet remains limited leading to similar loading on the winglet. Figure 8 illustrate this behaviour for a XRF1 wing that have been stiffened (Not perfectly rigid). The pressure contours evidence that winglet loading is marginally affected by cant deflection.

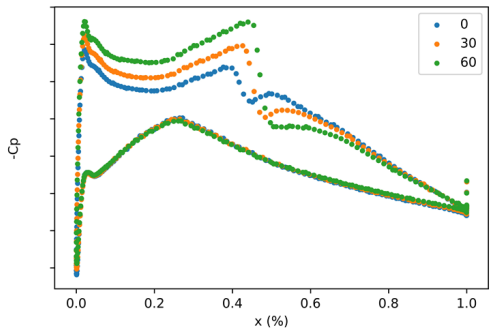

Figure 8: Pressure coefficient at 25% of winglet span for a rigid wing and three cant angles.

The consequence is that the normal force on the winglet barely changes while its orientation does. The lift it generates then drops, center of lift shifts inward and induced drag increases. This phenomenon is qualitatively illustrated in Fig.9a and the qualitative change in lift distribution is shown on Fig.9b for the stiffened XRF1 wing.

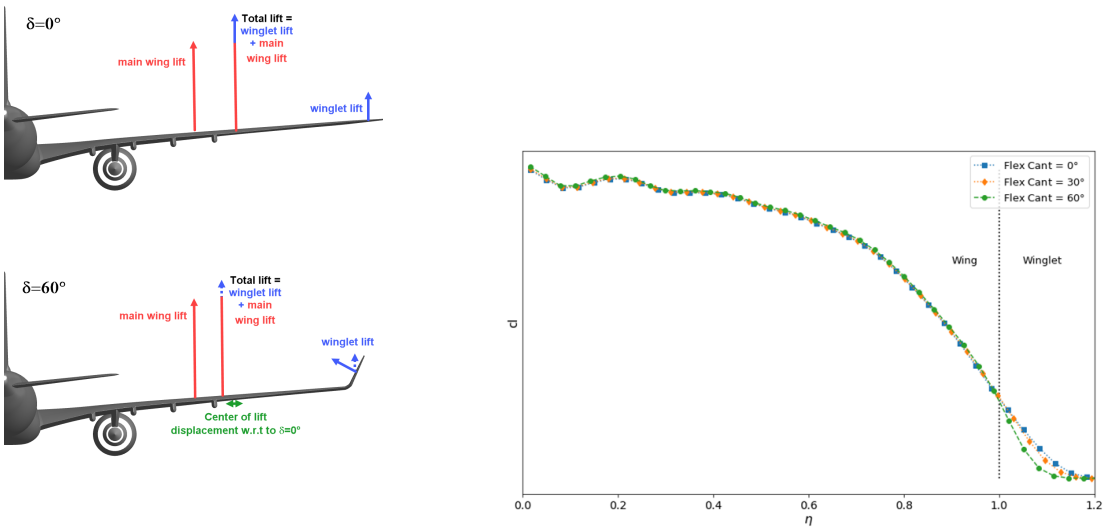

(a) Qualitative variation of winglet loading (b) Quantitative variation of lift distribution

Figure 9: Qualitative and quantitative visualisation of winglet loading variation and impact on lift distribution for rigid wings.

Adding flexibility impacts drastically the variation of local AoA on the winglet and consequently the lift it generates. Indeed, in that case rigid effects (2) and flexible effects (3) act conjointly. For sweptback wings, wing twist deformation is negative (nose down)

and is propagated to the winglet reducing its local AoA for small cant values. When winglet folds up or down, flexible effect vanishes and only rigid one persists. Local AoA increases noticeably and so does the loads on the winglet as illustrated in Fig.10. Because flexible effect reduces the local AoA for small cant deflection it appears on pressure contours that the winglet generates almost no load for $\delta = 0\,\text{deg}$. On the contrary, from $\delta = 30\,\text{deg}$ to $\delta = 60\,\text{deg}$ it increases significantly.

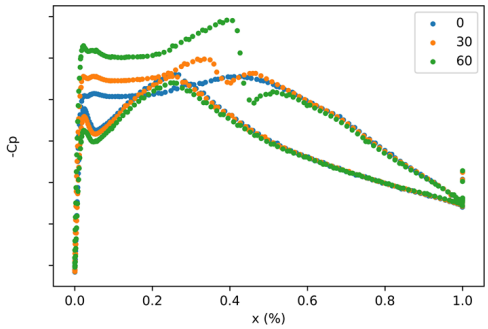

Figure 10: Pressure coefficient at 25% of winglet span for a flexible wing and three cant angles.

As winglet folds, the resultant aerodynamic force increases which compensates for the orientation change. Then lift remains the same within a range of cant variation. Once winglet loading increase is no more sufficient to balance force orientation modification the lift starts to drop. This phenomenon is illustrated in Fig.11a and Fig.11b. It clearly appears that until $\delta = 30\,\text{deg}$ the lift distribution barely change, then folding the winglet further has an impact on wing loading. As induced drag depends on lift distribution, its sensitivity to cant angle is reduced by flexible effects. The efficiency assessment of active winglet devices appears to be highly moderated by flexible effects and must be assessed using coupled approaches.

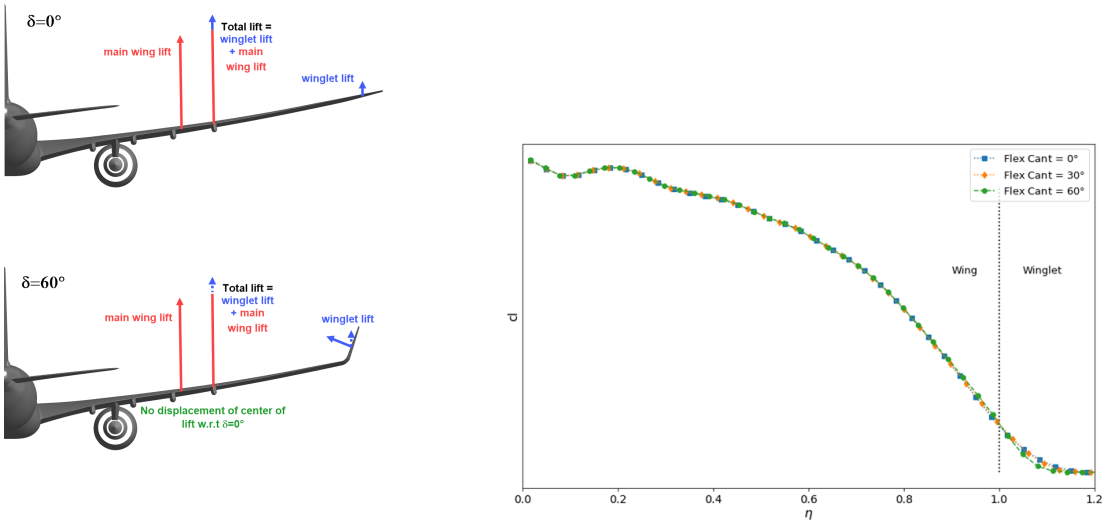

(a) Qualitative variation of winglet loading (b) Quantitative variation of lift distribution

Figure 11: Qualitative and quantitative visualisation of winglet loading variation and impact on lift distribution for flexible wings.

A similar reasoning applies to explain the dependency of active winglet efficiency on mean flight altitude as highlighted in Fig.7b. For low flight levels and a given aircraft weight, AoA is lower than for high flight levels. Therefore, considering (2) + (3) the flexible effect dominates. Particularly, local AoA on winglet may increase by almost 2 deg when it folds as illustrated in Fig.12a. In Fig.12b this variation appears to be damped to around 0.8 deg for higher altitudes.

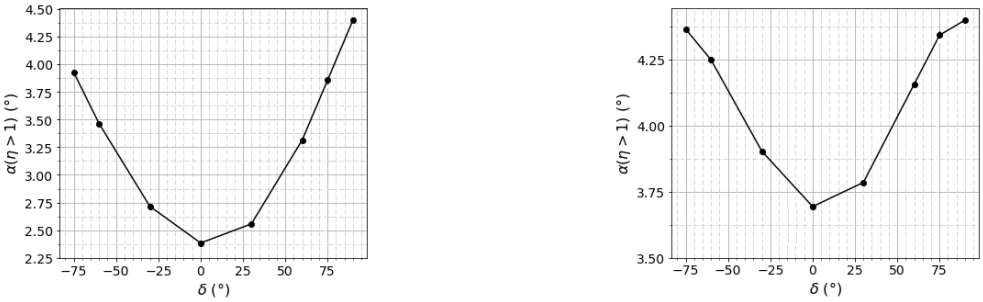

(a) Low cruise altitude. (b) High cruise altitude

Figure 12: Evolution of local angle of attack at winglet tip with cant angle for different flight altitudes.

At low flight levels, as shown is Fig.13 the winglet barely generates lift independently of the XRF1 configuration considered. As cant angle absolute value increases, larger loads are observed on the winglets that are sufficient to make lift distribution shift outward as highlighted by Fig.15. The actuation of the winglet has beneficial implication on drag in that conditions.

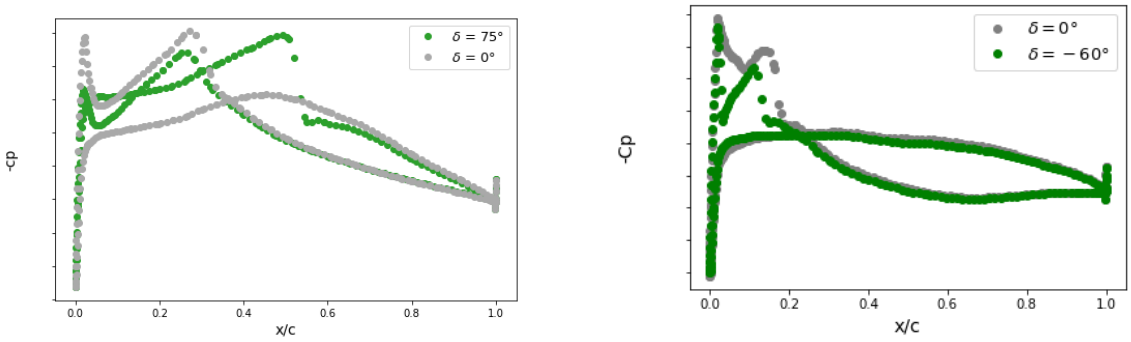

(a) XRF1 retrofitted with winglets. (b) XRF1 high aspect ratio

Figure 13: Winglet loading for two different cant deflections at low cruise altitude for the two XRF1 test cases.

Increasing the altitude means increasing $\alpha_{winglet_r}$ predominance in front of flexible effects. Loading on winglet keep on increasing as it folds as illustrated in Fig.15a but not sufficiently to compensate the change in resultant force orientation. The lift then shifts inward as in Fig.15b and optimal deflection lies in the vicinity of $\delta = 0$ deg. Small benefits are then expected from winglet actuation.

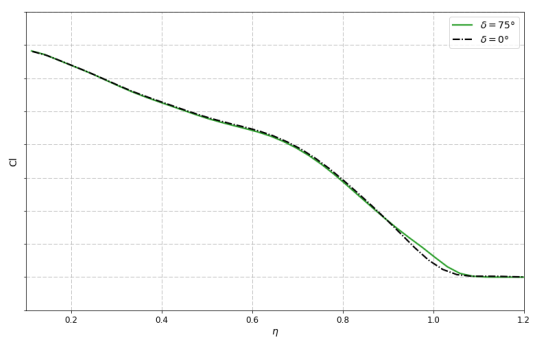

(a) XRF1 retrofitted with winglets.

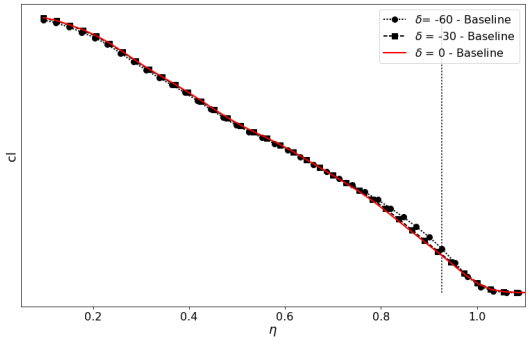

(b) XRF1 high aspect ratio

Figure 14: Lift distribution for two different cant deflections at low cruise altitude for the two XRF1 test cases.

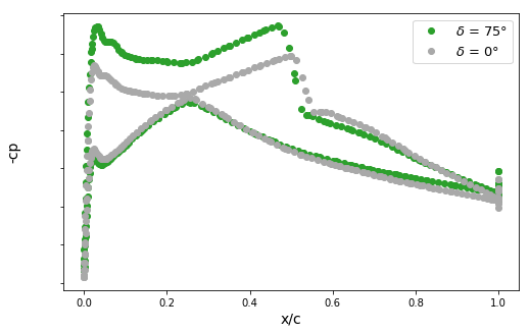

(a) Pressure contour at 25% of winglet span

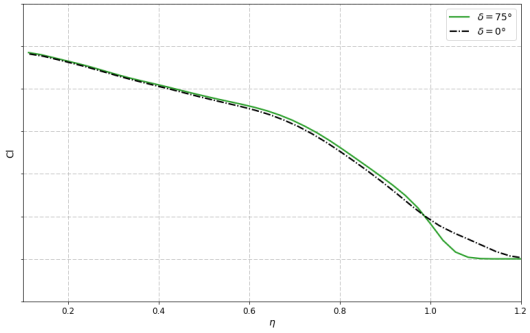

(b) Spanwise lift distribution

Figure 15: Pressure contour and lift distribution for high altitude flight illustrate effect of altitude on winglet loading and aircraft performances.

4 IMPLICATIONS ON FLUTTER BOUNDARIES

Moving masses at the tip of the wing may have consequences on the dynamic response of the structure and particularly on aeroelastic stability that must be assessed. It must be ensured that the flutter critical speed remains larger than the diving speed with a safety margin of 15% in the whole flight domain and whatever the winglet cant deflection.

4.1 Impact of cant variation on modes

First, a parametric modal analysis is performed for the XRF1 high aspect ratio wing. The configuration with retrofitted winglet is not presented here because it exhibits significant margins to flutter that could not be totally be erased by winglet actuation. Seven cant angles are analysed from -90 deg to 90 deg. The sensitivity to active winglet size is also considered by changing the hinge location. A winglet of 2m and a larger one of 4m are analysed.

The frequency evolution with cant angle of the six first structural modes is plotted in Fig.16a and in Fig.16b for the smaller and the larger winglet respectively.

From Fig.16a it can be noticed that mode 4, 5 and 6 frequencies vary by more than 5% when cant angle absolute value increases from $\delta = 0$ deg to $\delta = 90$ deg. Particularly, larger variations occur above $|\delta| = 30$ deg. On the contrary the first three modes frequencies are less impacted by cant changes.

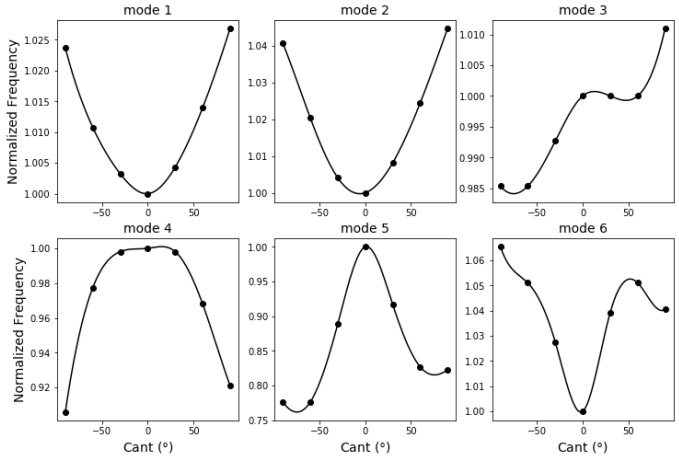

(a) Small winglet

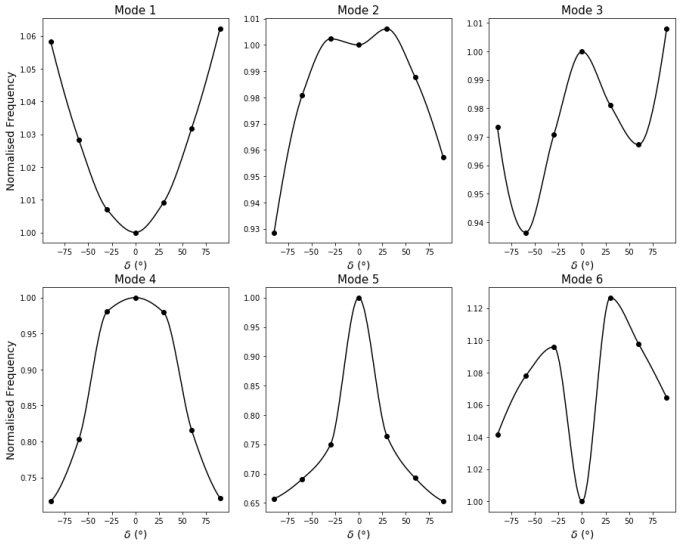

(b) Large winglet

Figure 16: First six structural modes frequency variations with cant angle for two winglet sizes.

Observing the evolutions for the larger winglet in Fig.16b shows that this behaviour is exacerbated and that all modes are impacted by large frequency variation with cant angle. Particularly, mode 2 frequency drops by 7%, mode 4 one by more than 25% and mode 5 by almost 35%.

The observation of the mode shapes for extreme cant deflections ($\delta = 0\,\text{deg}$ and $\delta = 90\,\text{deg}$) provides deeper insight into the phenomenon at stake. From Fig.17 it can be noticed that the nature of the three first modes remains unchanged. Namely, the 1 node bending, 2 nodes bending and 1 node fore-and-aft modes occur in first, second and third position respectively. On the other hand, the first torsion mode that appears in sixth position for $\delta = 0\,\text{deg}$ switches to fourth position when $\delta = 90\,\text{deg}$. In the meantime, the 3 nodes bending and 2 nodes fore-and-aft modes move backward respectively to fifth and sixth position. This alteration of the mode nature when cant angle varies is the cause for the modes frequencies to change abruptly.

The same occurs for the larger winglet but the change is even more pronounced. In-

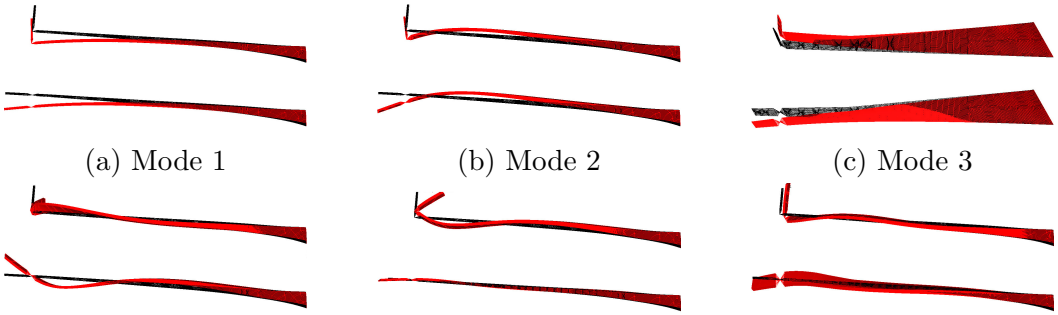

(a) Mode 1 (b) Mode 2 (c) Mode 3

(d) Mode 4 (e) Mode 5 (f) Mode 6

Figure 17: Small winglet first six structural mode shapes for $\delta = 0\,\text{deg}$ and $\delta = 90\,\text{deg}$.

deed, observing Fig.18 it appears that the first torsion mode switches from sixth position to second one when winglet folds passing through fourth position when $\delta \approx 30\,\text{deg}$ (not plotted here). Simultaneously the other modes move backward similarly to the observations made for the smaller winglet. This displacement of the first torsion mode within the mode sequence causes the fourth mode frequency to decrease slightly between $|\delta| = 0\,\text{deg}$ and $|\delta| = 30\,\text{deg}$ before to drop rapidly for further deflections. The second mode remains a bending mode till $|\delta| > 30\,\text{deg}$ then the frequency falls when it switches to torsion.

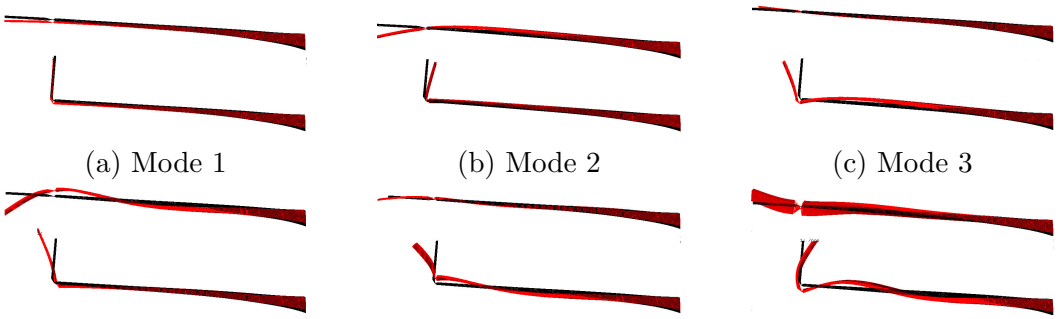

(a) Mode 1 (b) Mode 2 (c) Mode 3

(d) Mode 4 (e) Mode 5 (f) Mode 6

Figure 18: Large winglet first six structural mode shapes for $\delta = 0\,\text{deg}$ and $\delta = 90\,\text{deg}$.

4.2 Consequences on flutter onset

The alteration of the mode sequence that has just been evidenced is not without consequences on flutter onset. The instability occurs when torsion and bending modes couple. If torsion frequency falls while bending one increases slightly as it is figured in Fig.16 flutter is more prone to be triggered. As a results the flutter speed diminishes as winglet deflects upward or downward.

Figure 19 shows a reduction of almost 20% of the flutter critical speed for the smaller winglet and more than 35% for the larger one. The figure also highlights the modes involved in the coupling, it clearly shows that the change in the mode sequence is the main responsible for the dramatic degradation of flutter characteristics.

5 CONCLUSIONS

In this paper the active winglet efficiency is assessed for a high aspect ratio configuration of the XRF1 test case and compared to values from previous studies on XRF1 retrofitted

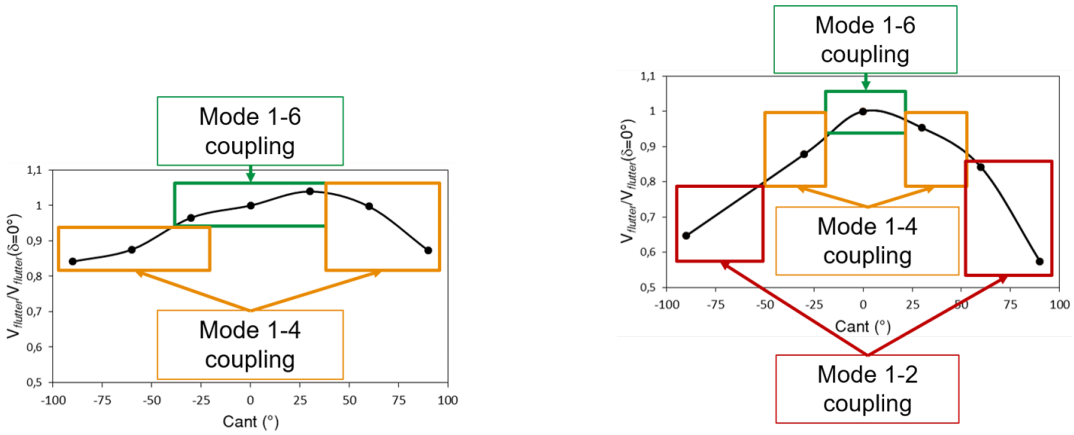

(a) Small winglet (b) Large winglet

Figure 19: Flutter speed variation with cant angle for two active winglet sizes.

with optimised winglet. It reveals that the similar fuel savings are achievable with this technology independently of the configuration considered. This benefits are much lesser than those found in the literature so far. The explanation lies in the consideration of static aeroelastic deformation in this study while the technology was only assessed through aerodynamic computation. It is shown that wing deformation plays a center role in the variation of lift on the winglet and consequently on its distribution over the wing. Particularly it is demonstrated that for flexible wings winglet is less loaded for small cant angles than large ones leading small variation of lift when the winglet folds. The drag sensitivity to cant is then reduced and so does the device efficiency. This paper also analyses the implication of folding a winglet on flutter onset. It is shown that mode sequence is profoundly affected by the variation of winglet cant angle. It results that the torsion mode frequency drops as winglet folds. This favours coupling with bending modes and degrade the flutter stability. It is particularly shown that critical speed drops by 20 to more than 35% depending on the moveable part size.

REFERENCES

[1] L. Prandtl. Theory of lifting surfaces. Technical Note 9, NACA, 1920.

[2] R. Faye, R. Laprete, and M. Winter. Blended winglet for improved airplane performance. *Boeing Aero Magasin*, (17):16–31, 2002.

[3] R. T. Whitcomb. A design approach and selected wind-tunnel results at high subsonic speed for wing-tip mounted winglets. Technical Note 8260, NASA Langley Research Center, 1976.

[4] A. Castrichini, V. H. Siddaramaiah, D. E. Calderon, J. E. Cooper, T. Wilson, and Y. Lemmens. Preliminary investigations of use of flexible folding wing tips for static and dynamic load alleviation. *The Aeronautical Journal*, 121(1235):73–94, 2016. doi:10.1017/aer.2016.108.

[5] W. R. Kruger, J. Dillinger, R. D. Breuker, and K. Haydn. Investigations of passive wing technologies for load reduction. *CEAS Aeronautical Journal*, 10(4):77–93, 2019. doi:10.1007/s13272-019-00393-2.

[6] G. Moy, C. E. Jokisch, M. S. Good, M. J. Gardner, M. E. Renzelmann, and J. C. Houten. Folding wing system, 2017. US Patent 2017/0349296.

[7] R. P. Liem, G. K. W. Kenway, and J. R. R. A. Martins. Multimission aircraft fuel-burn minimization via multipoint aerostructural optimization. *AIAA Journal*, 53(1): 104–122, 2014. doi:10.2514/1.J052940.

[8] S. Vasista, L. Tong, and K. C. Wong. Realization of morphing wings: A multidisciplinary challenge. *Journal of Aircraft*, 49(1):11–28, 2012. doi:10.2514/1.C031060.

[9] D. A. Burdette, G. K. Kenway, and J. R. R. A. Martins. *Aerostructural design optimization of a continuous morphing trailing edge aircraft for improved mission performance*. 2016. doi:10.2514/6.2016-3209.

[10] N. Nguyen, U. Kaul, S. Lebofsky, E. Ting, D. Chaparro, and J. Urnes. *Development of Variable Camber Continuous Trailing Edge Flap for Performance Adaptive Aeroelastic Wing*. 2015. doi:10.2514/6.2016-3209.

[11] C. Concilio and L. Lecce. Historical background and current scenario. *Morphing Wing Technologies*, 49(1):3–84, 2012.

[12] B. Barriety. Aircraft with active control of the warping of its wings, 20104. US Patent 62827314B2.

[13] M. Delavenne, B. Barriety, F. Vetrano, V. Ferrand, and M. Salaun. *Parametric Analysis of an Active Winglet Concept for High Aspect Ratio Wing Using CFD/CSM Computations*. 2020. doi:10.2514/6.2020-2662.

[14] M. Delavenne, B. Barriety, F. Vetrano, V. Ferrand, and M. Salaun. *A Static Aeroelastic Analysis of an Active Winglet Concept for Aircraft Performances Improvement*, pages 77–82. Springer Singapore, Singapore, 2020. ISBN 978-981-33-4960-5.

[15] M. Delavenne, B. Barriety, F. Vetrano, V. Ferrand, and M. Salaun. Assessment of the efficiency of an active winglet concept for a long-range aircraft. *CEAS Aeronautical Journal*, 11(4):971–990, 2020. doi:10.1007/s13272-020-00465-8.

[16] J. E. Cooper, I. Chekkal, R. Cheung, C. Wales, N. J. Allen, S. Lawson, A. J. Peace, R. Cook, P. Standen, S. D. Hancock, and G. M. Carossa. Desing of a morphing wingtip. *Journal of Aircraft*, 52(5):1394–1403, 2015. doi:10.2514/1.C032861.

[17] G. K. W. Kenway and J. R. R. A. Martins. High fidelity aerostructural optimization of the airbus xrf1 aircraft configuration. Technical report, Airbus Operations SAS, 2016.

[18] *Technical documentation of the DLR TAU-Code release 2013.1.0*. Deutsches Zentrum fur Luft und Raumfhart, 2013.

[19] R. Thormann and M. Widhalm. Linear-frequency-domain predictions of dynamic-response data for viscous transonic flows. *AIAA Journal*, 51(11):2540–2557, 2013. doi:10.2514/1.J051896.

[20] G. X. Dussart, M. M. Lone, C. O'Rourke, and T. Wilson. *In-flight Folding Wingtip System: Inspiration from the XB-70 Valkyrie*. 2019. doi:10.2514/6.2019-1855.

[21] M. Software. Msc nastran, multidisciplinary structural analysis. Website, 2021. URL `https://www.mscsoftware.com/fr/product/msc-nastran`.

[22] H. J. Hassig. An approximate true damping solution of the flutter equation by determinant iteration. *Journal of Aircraft*, 8(11):885–889, 1971. doi:10.2514/3.44311.

[23] A. I. J. Forrester, A. Sóbester, and A. J. Keane. *Constructing a Surrogate*, chapter 2, pages 33–76. John Wiley & Sons, Ltd, 2008. doi:10.1002/9780470770801.ch2.

[24] D. R. Jones. A taxonomy of global optimization methods based on response surfaces. *journal of Global Optimization*, 21(4):345–383, 2001. doi:10.1023/A:10127710255751.